Chapter 9
Ultrafast Nanoplasmonic Photoemission

Péter Dombi

Abstract The interaction of ultrashort laser pulses with plasmonic nanostructures enables the extreme, unprecedented localization of electromagnetic fields in both space and time. Ultrashort plasmonic fields can be bound to the closest nanoscale vicinity of nanoparticles and thin films and this way, new aspects of fundamental photoemission and other electron phenomena can be demonstrated. Here, we will review these phenomena including strong-field nanoplasmonic photoemission and keV electron acceleration on the nanoscale.

9.1 Introduction

9.1.1 Introduction to Surface Plasmon Enhanced Electron Phenomena

Intense ultrashort pulses of laser light have been exploited in a number of fundamental interaction studies involving strong electromagnetic fields and atoms/molecules. These interactions laid the foundations of, for example, femtochemistry and attophysics, representing prominent examples in this field. For all of these cases, the femtosecond laser beam needs to be focused onto a target where the minimum achievable interaction volume is limited by diffraction. When ultrashort pulses impinge on atomic and/or molecular samples, this volume is typically some cubic microns. This also caps the maximum achievable on-target intensity. If a free-space laser beam could be confined to well below the wavelength scale, the benefit would be an increased spatial resolution in applications, moreover, enhanced electromagnetic fields at nanoscale interaction volumes could be achieved. A solution for this challenge is readily offered by surface plasmons induced by field-driven charge oscillations in metallic nanolayers or nanostructures. The advantage offered by these

P. Dombi (✉)
MTA "Lendület" Ultrafast Nanooptics Group, Wigner Research Centre for Physics,
Konkoly-Thege M. út 29-33, Budapest 1121, Hungary
e-mail: dombi.peter@wigner.mta.hu

configurations is twofold: (i) they offer the sub-wavelength confinement of the electromagnetic field and (ii) this way substantial enhancement of the nano-localized electric field can be achieved with respect to that of a focused laser pulse.

Several fundamental physical phenomena show new aspects when the interaction is taking place in nano-localized fields. Here, we will review the recently discovered new facets of electron emission from metals with the help of ultrashort laser pulses and plasmonic nanostructures. The advancement of femtosecond laser technology together with increased research on nanoemitters enabled these fundamental discoveries. We will also show some routes towards the application of these unique, ultrafast photoemission phenomena.
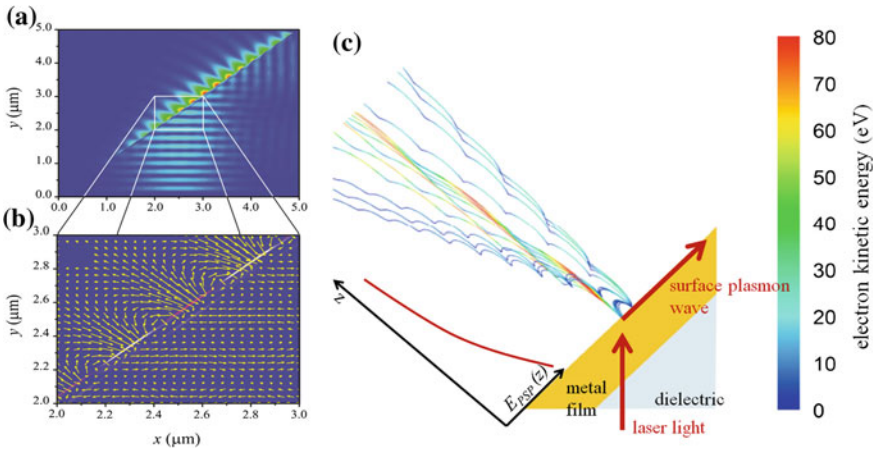
9.1.2 Surface Plasmons

It was observed early that the efficiency of many chemical and physical processes involving laser-surface interactions can be significantly enhanced by the nanoscale roughness of the metal surface involved. These processes and applications include Raman scattering [1], plasmonic biosensors [2], and some nonlinear optical phenomena such as surface-harmonic generation [3, 4] and optical rectification [5]. A rough surface that can provide such a signal enhancement is a random, nanostructured, metallic surface which facilitates an electric field enhancement and surface plasmon coupling. It is both metal films and the nanoscale voids and protrusions of these materials that can support plasmons. Therefore, it is important to introduce basic phenomena related to the generation of these electromagnetic fields.

Surface plasmons are charge-density oscillations of conduction band electrons found in thin metal films or nanoparticles (Fig. 9.1). For metal films, these oscillations can support propagating waves on the metal film (propagating surface plasmons, (PSPs), whereas for nanoparticles the oscillations typically remain localized to the nanoparticle vicinity (localized surface plasmons, LSPs). Surface plasmons are well known to confine electromagnetic energy to nanoscale spatial domains [6] and thus they can possess higher electric field strengths than that of the laser responsible for their generation in both cases. This opens the possibility of using ultra-compact, table-top, low-power lasers for inducing strong-field light-matter interactions in highly confined surface plasmon fields.

The simplest means of producing PSPs is by way of the Kretschmann-Raether coupling geometry (Fig. 9.1). A thin metal film (ca. 40–70 nm thick) coats the hypotenuse face of a right-angle prism. After satisfying the momentum-matching resonance condition at a certain angle of incidence, the incoming laser field becomes evanescently confined to a nanoscale surface layer (some 200–300 nm in width) at the surface of the thin film. The electromagnetic near field at the metal-air or metal-vacuum boundary decays exponentially away from the interface [6]. Even though lateral dimensions of the PSP on the surface correspond to a diffraction-limited focal spot size, the remaining one-dimensional field nanoconfinement is sufficient to induce both surface plasmon enhanced photoemission and electron acceleration. These phenomena
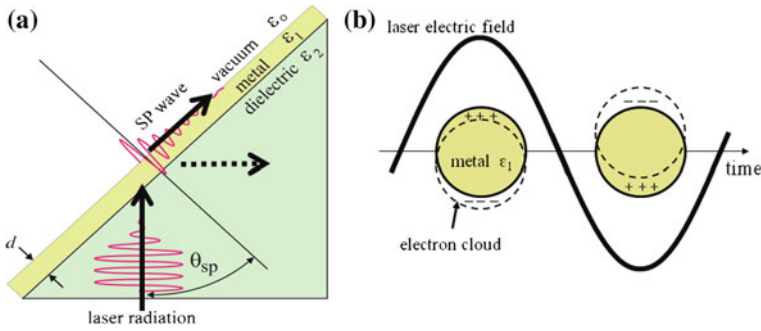
Fig. 9.1 Surface plasmon coupling of free-space electromagnetic waves in **a** Kretschmann-Raether configuration at a specific resonant incidence angle θ_{SP} and with **b** metal nanoparticles where the electron cloud can be seen moving collectively under the influence of the laser field. The generated surface bound electromagnetic wave in (**a**) is called a propagating surface plasmon (PSP), whereas in (**b**) localized surface plasmon oscillation (LSP) is induced. *Arrows* in (**a**) indicate the flow of energy. In case of perfect PSP coupling, the reflected beam from the metal surface indicated by the *dashed arrow* disappears

Fig. 9.2 **a** Electric field distribution of a propagating surface plasmon wave on a metal nanolayer in the Kretschmann-Raether coupling geometry. **b** Depicts electric field vectors. *Source* [16]. **c** Illustrates the trajectories of photoemitted electrons in the PSP field and the ponderomotive, cycle-by-cycle acceleration process in the inhomogeneous field for some sample electron trajectories

will be detailed below. Typical electric field distribution of a PSP is visualised in Fig. 9.2a, b.

The other form of surface plasmon generation uses localized charge oscillations in metal nanoparticles induced through the application of an external optical field, so-called localized surface plasmons (LSPs, see Fig. 9.1b). Certain metal nanoparticles can sustain LSPs, which exhibit a pronounced resonance behavior coming together

with strongly localized, evanescent fields [7, 8]. The combination of the sharp optical resonance condition and sub-wavelength field localization [6] renders these particles ideal for various applications, including (bio)sensors [9], optoelectronics [10, 11] and photovoltaics [12].

9.2 Novel Nanoplasmonic Photoemission Phenomena

The nanoconfinement property of plasmonic fields has remarkable consequences, as already observed for some applications [1–4]. Moreover, enhancements in photo-electron emission quantum efficiency by more than three orders of magnitude have been observed in the presence of PSP excitation from noble metal films using the Kretschmann-Raether configuration [14, 15] compared to non-plasmonic photo-emission yields from metal surfaces. Other intriguing photoemission phenomena both in PSP and LSP fields will be detailed below after reviewing basic photoemission processes upon laser-solid interaction.

9.2.1 Linear Versus Nonlinear Photoemission and Photocurrents

Electron emission from a metal can take place in various forms depending on the intensity and wavelength of the interacting light. Here, we will introduce this process from the point-of-view of its linearity. In the next section we will analyse different types of nonlinear photoemission phenomena, as well.

In the linear photoelectron emission (in short, photoemission) regime, a single photon interacts with an electron in the metal to excite it to the vacuum niveau. Provided that the energy of the photon is higher than the work function of the metal, the photoemission process is linear, since one photoemitted electron stems from an incident photon. Since typical metal work functions are a few electronvolts, linear photoemission can be induced by ultraviolet photons, and the number of photoelectrons is directly proportional to the intensity of the incoming light.

On the other hand, for intense optical fields in the visible spectrum (when the energy of each individual photon is lower than the work function of the metal), nonlinear photoemission can still take place where the joint action of multiple photons is needed to set one electron free. One example is when nonlinear photoemission occurs in the form of the simultaneous, non-sequential absorption of several photons by the metal film. In these cases, the number of photoelectrons no longer scales linearly with the intensity of the light source. Some types of these phenomena will be reviewed below, after introducing basic scale parameters of these interaction processes.

Photocurrents from metal surfaces can be generated with or without the presence of surface plasmons. In the presence of plasmons, their electric field (and not that of the laser pulse) must to be considered when describing the photoemission currents.

9.2.2 Scale Parameters in Photoemission Processes

Simple equation of motion considerations yield that the average oscillation energy of a free electron in the field of an infinite electromagnetic plane wave is

$$U_p = \frac{e^2 E_l^2}{4m\omega^2} \tag{9.1}$$

where the electron charge and rest mass are denoted by e and m, respectively. ω is the angular frequency, and the amplitude of the electric field strength of the laser light is given by E_l.

Fields that are inhomogeneous in space change this picture only slightly. For example, in case of a laser pulse which is focused, U_p can be generalized by taking the spatial dependence into account: $U_p \rightarrow U_p(\mathbf{r})$ following the spatial variation of the electric field amplitude, $E_l(\mathbf{r})$. The generalized $U_p(\mathbf{r})$ quantity is commonly called the ponderomotive potential, as the cycle-by-cycle motion of an electron in such an oscillating field follows the gradient of $U_p(\mathbf{r})$, (see Fig. 9.2c). The ponderomotive potential determines the cycle-by-cycle motion and gradual energy gain of a free electron in a spatially inhomogeneous laser field. In addition, this quantity also proved to be very useful for the distinction between different regimes of nonlinear photoemission from metals (as well as photoionization from atoms).

The analysis of Keldysh yielded a famous perturbation parameter, γ that is an efficient scale parameter to describe bound-free transitions (e.g., photoemission, tunneling) in a general way that are induced by laser fields. This adiabaticity parameter is defined as

$$\gamma^2 = \frac{W}{2U_p} = \left(\frac{\omega\sqrt{2mW}}{eE_l}\right)^2 \tag{9.2}$$

where W is the work function of the metal. It can be shown that photoemission from metals and photoionization mechanisms are distinctively different for $\gamma \gg 1$ (low laser intensities) and $\gamma \ll 1$ (high laser intensities), to be discussed below.

9.2.3 Mechanisms of Photoemission and Related Phenomena

The distinction between photoemission phenomena depends on the extent of distortion of the metal surface potential by the external laser field. Here, we will classify these processes in three different categories, making a distinction between (i)
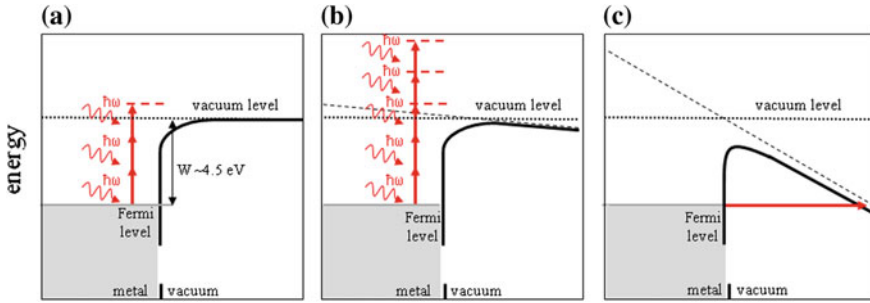
Fig. 9.3 Mechanisms of photoelectron emission for different laser intensities. **a** For low laser intensity, the simultaneous action of multiple photons can set an electron free. **b** By increasing the laser intensity, the metal surface potential becomes slightly distorted by the contribution of the laser field (*dashed line*). The dominant photoemission mechanism is still the absorption of multiple photons but in this case, more photons than the necessary minimum can interact with the electron. This phenomenon resulting in higher final electron kinetic energies is called above threshold photoemission. **c** When the laser field is strong enough to distort the potential substantially, direct tunnelling of an electron from the Fermi level is possible. This phenomenon is called tunnelling or strong-field photoemission

multi-photon-induced photoemission, (ii) above threshold photoemission and (iii) tunneling or strong-field emission, schematically illustrated in Fig. 9.3.

9.2.3.1 Multi-photon Induced Nanoplasmonic Photoemission and Applications

When the value of the Keldysh parameter is $\gamma \gg 1$, meaning low intensities (i.e., where the field of the laser pulse is not sufficient to significantly distort the binding potential), multi-photon-induced processes dominate at visible wavelengths (Fig. 9.3a). These nonlinear processes can be described by a perturbative approach since the incident laser field represents only a perturbation term in the Hamiltonian describing the system. As such, the interaction of light with matter is predominantly non-adiabatic and it is governed by the evolution of the amplitude of the laser field, or, in other words, the intensity envelope of the laser pulse. In the case of metals (4–6 eV work function), multi-photon-induced photoemission typically takes place with visible or near-infrared light (1–3 eV photon energy) with 2–5 photons needed to generate one emitted electron. The energy balance of this n-photon process can be described by

$$n\hbar\omega = E_{\text{kin}} + W \tag{9.3}$$
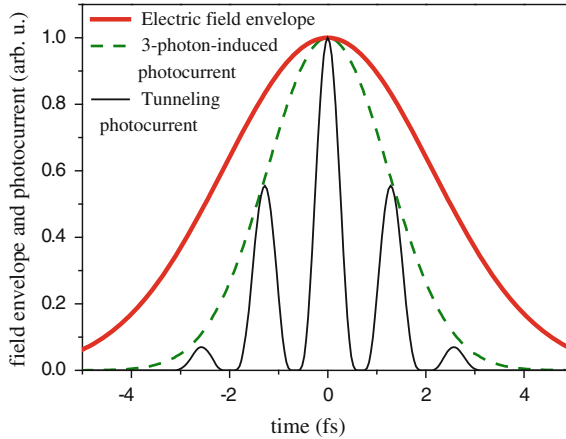
Fig. 9.4 Examples of electron emission temporal profiles for a few-femtosecond laser pulse with a duration of 3.5 fs (intensity full width at half maximum (FWHM)). The *thick solid curve* depicts the field envelope evolution. The *dashed curve* is the photocurrent temporal distribution in case of a three-photon-induced photoemission according to formula (9.4). The *thin solid curve* is the photocurrent profile in case of tunneling electron emission from the surface, determined by the Fowler-Nordheim equation (for further details, see text)

with E_{kin} being the kinetic energy of the photoemitted electron, W representing the work function to be overcome by the simultaneous action of n photons with $\hbar\omega$ energy each. In this case, we can assume that the evolution of the surface photocurrent $j(t)$ is proportional to the nth power of the intensity of the laser field:

$$j(t) \propto I^n(t) \tag{9.4}$$

This relationship yields a very good approximation of the temporal profile for multi-photon-induced photoemission, as confirmed by a full quantum mechanical description of the process [17]. In this case, it is the instantaneous amplitude of the field oscillation which determines the emission probability (illustrated in Fig. 9.4), for a Gaussian laser pulse intensity profile, $I(t)$, the electron emission curve, $j(t)$, has a full width at half maximum (FWHM) that is $\sqrt{n}$ times shorter than the FWHM of the original $I(t)$ curve. Measuring the photocurrent as a function of laser intensity and plotting this curve on a double logarithmic scale enables easy determination of the exponent n by measuring the slope of this curve.

The inherent field enhancement of surface plasmons enables the generation of significantly enhanced photocurrents from plasmonic samples. Since it is the surface plasmon field that matters for determining the total photocurrent, (9.4) suggests huge photocurrent enhancement even for moderate field enhancement factors. Systematic studies with plasmonic Au, Ag, Cu, and Al thin films revealed photoemission yield enhancement factors of $\times 50 \ldots \times 3500$ (or field enhancements of between
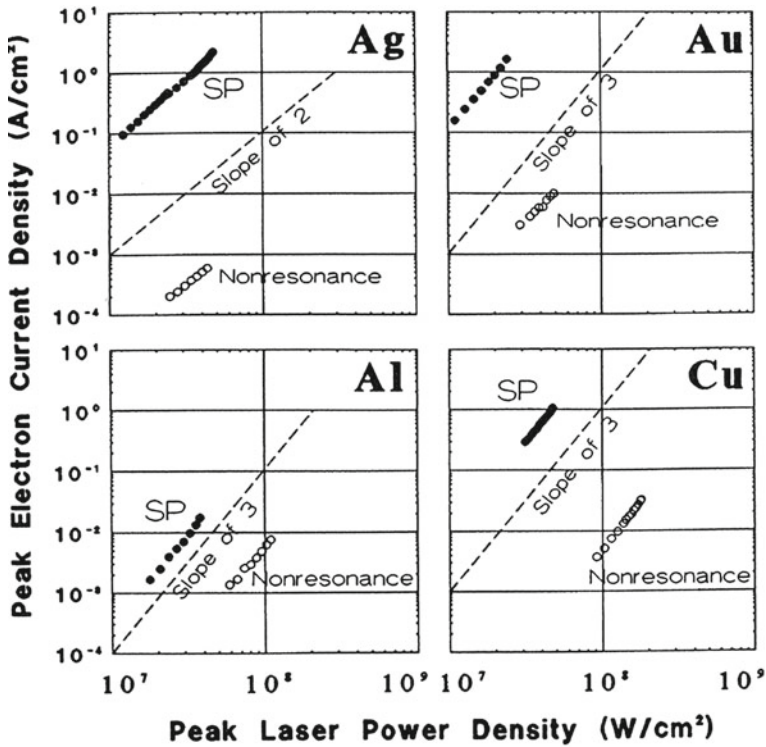
Fig. 9.5 The enhancement of PSP-induced multi-photon photoemission yield as a function of the intensity of the incident laser beam for four different surfaces plotted on double logarithmic scales. The slope of each linear fit equals the nonlinearity of the photoemission process. The lower data sets marked as "nonresonance" depict photoelectron yield from the same metal film without PSP coupling but with a similar illumination geometry. The substantial increase of the PSP-enhanced photoelectron yield is clearly illustrated with the *upper curves* plotted with *solid symbols* and marked with "SP". *Source* [15]

×2 and ×8) [15] as depicted in Fig. 9.5. The curves show the intensity dependence of the photoelectron yield on double logarithmic scales. Therefore, the slope of each linear fit equals the degree of nonlinearity of the photoemission process. It can be seen (since there is no deviation from the linear fits) that multi-photon-induced emission is the only contributing mechanism to the photoemission process. To estimate the magnitude of plasmonic field enhancement, the PSP-induced photoelectron yield was compared to nonlinear photoemission without PSP coupling in the same film.

The fact that the electron yield is much higher with PSP coupling than with direct surface illumination without PSP coupling underlines a very important feature of the process, namely that it is the field of surface plasmons that induces the observed photocurrent.
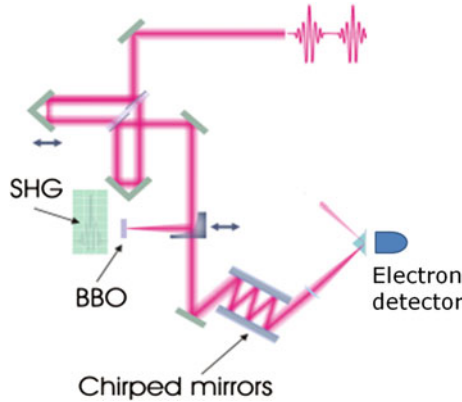
Fig. 9.6 Experimental scheme for time-resolved measurement of ultrashort surface plasmon wavepackets. Laser pulses with 5 fs duration are entering the setup with 5 nJ pulse energy. After passing through an interferometer they can be either characterized by a beta-barium-borate (*BBO*) crystal by second harmonic generation (*SHG*) autocorrelation. Alternatively, by removing the parabolic focusing mirror, the interferometer output is focused onto a prism to generate PSPs. Pulse propagation in the prism material was pre-compensated for by introducing broadband chirped mirrors. Nonlinear autocorrelation of the PSP wavepacket is detected in vacuum by recording the plasmonic photoemission current as a function of the delay in the interferometer. *Source* [19]

The nonlinearity of plasmonic photoemission offers an additional benefit for the investigation of dynamical processes of PSPs. Because of the rather high, third or fourth order nonlinearity, autocorrelation-type measurements can be carried out with the help of photoemitted electrons. This provides valuable information on the dynamics in the metal [18], moreover, if the multiphoton photoemission process is induced by surface plasmon fields, such nonlinear dynamic measurements can reveal temporal information on PSP wavepackets [19]. Such a scheme is illustrated in Fig. 9.6.

The plasmonic sample is placed after an interferometer where the delay between the arms can be changed. Plasmonic photocurrent is measured as a function of this delay. This way, the setup acts a higher order autocorrelator, the nonlinearity of which is dependent on the order of the multi-photon-induced electron emission process. It is, however, the plasmonic field which induces photoemission, not that of the laser pulse. This way, temporal characterization of ultrashort PSP wavepackets can be performed, similarly to the autocorrelation characterization of an ultrashort laser pulse.

This concept was recently implemented experimentally [19] and results are depicted in Fig. 9.7. The photon order in the photoemission process was found to be 4 and it is indeed a fourth order autocorrelation function of a short pulse that is measured (Fig. 9.7a) with the method described above. This already indicates the few-cycle nature of the PSP wavepacket. Further analysis and comparison with calculated autocorrelation functions of the independently characterized laser pulse (Fig. 9.7b) resulted in a retrieved PSP wavepacket length of 6.5 fs [19]. It also has to be noted that such a broadband plasmonic wavepacket, of course, heavily spreads
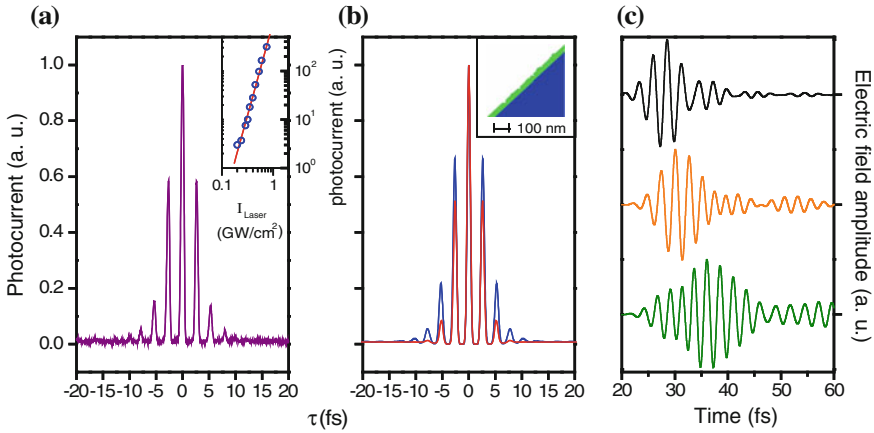
Fig. 9.7 **a** Measured interferometric time-resolved signal of PSP-enhanced photoemission induced by few-cycle pulses. The reconstructed *blue curve* in **b** is calculated using the simulation of PSP coupling on the actual, sputter-deposited metal film with 5-fs exciting laser pulses (see text for details and also the *inset* of **b** for the illustration of a part of the modeling geometry with the prism material in *blue* and the sputter-deposited silver film in *green*). The *red curve* in **b** is the calculated fourth-order autocorrelation function of the SPP-exciting, 5-fs laser pulse, plotted for reference. The *inset* of (**a**) illustrates the fourth-order dependence of the total PSP-induced, free-space photocurrent on a double logarithmic scale. The slope of the fit is n = 4.05 ± 0.11. The *curves* in (**c**) are typical, computed few-cycle SPP waveforms at different locations on the Ag surface exhibiting a 2.8 nm rms roughness. (*Source* [19])

upon propagation, the measured duration is only valid upon launching the PSP pulse. Independent, first-principles simulations of the whole experimental scheme (including a slight surface roughness of the metal film involved) was performed by solving Maxwell's equations for this problem. Results of this also confirm that the electric field waveforms at all points of the rough surface is indeed a few-cycle oscillation, hinting at the generation of few-cycle plasmonic wavepackets. They propagate along the line where PSPs are generated. These calculated waveforms at some representative parts of the surface are depicted in Fig. 9.7c.

With these experiments not only PSP field enhancement could be quantified with simple experimental methods, but time-resolved information could be gained on PSP dynamics. Multi-photon induced photoelectrons proved to be helpful tools in achieving both of these goals.

9.2.3.2 Above Threshold Photoemission with Nanoemitters

At slightly higher intensities than that needed for multi-photon-induced photoemission, it is also possible that a larger number of photons are absorbed than the minimum required. Figure 9.3b illustrates this case of above-threshold photoemission. This process, the likelihood of which decreases with the increasing number of absorbed

photons, is termed as "above-threshold photoemission" [20–24]. Above-threshold photoemission (ATP) bears close analogy to the well-known above-threshold ionization process taking place in atomic systems, discovered in 1979 [25].

In the decades since the discovery of above-threshold ionization, several efforts were made to demonstrate its metal surface analogy, ATP. Direct evidence of this process was not delivered since collective electron excitation, space-charge spectrum broadening and other adverse effects are known to smear electron spectra of extended surfaces illuminated by extended beams.

Eventually, one had to use nanoemitters to demonstrate such effects. Electrochemically etched metal nanotips enabled several fundamental discoveries in recent years [26–28]. The obvious demonstration of ATP for the first time was one of these [29]. Even though such nanotips do not typically exhibit plasmonic resonances, it is worth introducing this experiment here.

The experimental scheme and the results are depicted in Fig. 9.8. The illumination geometry of the sharp tungsten nanotip with a 8–10 nm radius of curvature is shown in Fig. 9.8a together with the whole experimental setup in Fig. 9.8b.

Measurement of the kinetic energy spectrum of the electrons emitted from a single tip nanoemitter show features with clear signs of ATP. Steps in the electron spectra in Fig. 9.8c are separated by exactly the photon energy ($\sim$1.5 eV). Moreover, the probability of the absorption of an additional photon decreases exponentially with the photon number, as expected from a perturbative high-order process. This is also evidenced by Fig. 9.8c. By increasing the intensity, higher-order processes become more likely, as intuition also suggests for the ATP case. Up to 9th order ATP can be
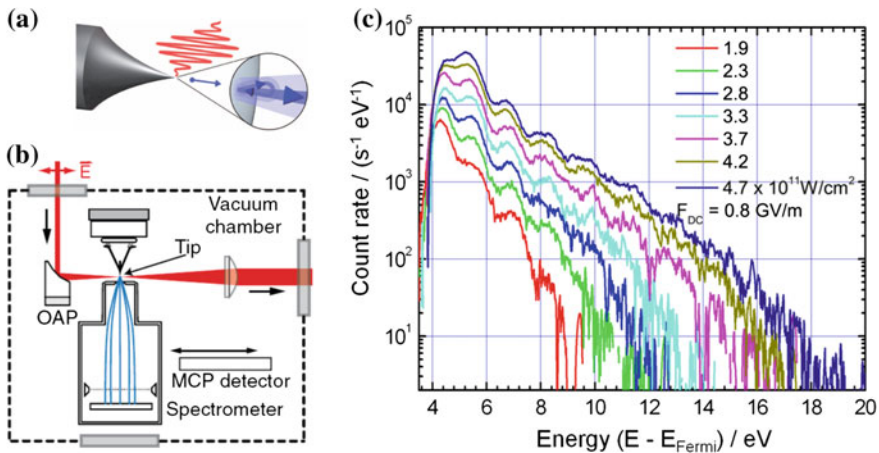
Fig. 9.8 **a** Sharp nanotip illuminated with ultrashort laser pulses. **b** Shows the experimental setup in which the kinetic energy spectrum of photoemitted electrons from a single nanotip can be measured. *OAP* Off-axis parabolic mirror, *MCP* Microchannel plate. Measured electron spectra for different incident laser intensities are shown in (**c**). Clear steps separated by the photon energy ($\sim$1.5 eV) can be observed in these spectra with the number of steps becoming higher with increasing laser intensity. This delivers proof for the above threshold photoemission process. *Source* [29]

observed for the highest intensities in this experiment, representing a clear advantage of the nanoemitter geometry over all previously used experimental schemes. The only disadvantage posed by non-plasmonic nanotips is the reduced field enhancement factor up to some 6–8 times based solely on the tip effect. Together with the limited set of shapes that can be realized with a nanotip, it is expected that future applications will rather be driven based on plasmonic nanoparticles.

9.2.3.3 Introduction to Strong-Field (Tunnelling) Photoemission

At higher interacting laser intensities than that needed for multi-photon-induced processes (including ATP), strong-field photoemission can also take place. This is characterized by the scheme in Fig. 9.3c with the electron being able to tunnel out from the metal. As opposed to the previous cases, where the photocurrent is typically governed by the field amplitude of the laser beam, here, the interaction is determined by the instantaneous field strength of the laser pulse (or, equivalently, of the surface plasmon field). Photocurrent generated in this way follows the field evolution of the pulse envelope instantaneously, without any cycle-averaging effects and without any delay. Therefore, this process is also termed as adiabatic emission. This interaction type is a well-known phenomenon that occurs within the context of photoionization of atoms in intense laser fields, representing the first step, for example, in a high harmonic generation process.

Field emission electron currents can be approximated by more complex formulae than multi-photon-induced emission. Approaches to deliver a closed-form analytic expression are based on various quantum mechanical tunnelling considerations. The formula most commonly applied in the literature to metals (for both static and oscillating laser fields) is the Fowler-Nordheim equation [30, 31]. The electric field dependence of the tunneling current is described by

$$j(t) \propto \frac{e^3 E_l(t)^2}{8\pi h W t^2(w)} \exp\left(-\frac{8\pi\sqrt{2m}W^{3/2}}{3he\,|E_l(t)|}v(w)\right) \tag{9.5}$$

where $E_l(t)$ denotes the laser field strength, e and m the electron charge and rest mass respectively, and h is Planck's constant. W is work function of the metal, $v(w)$ is a slowly varying function taking into account the image force of the tunneling electron with $0.4 < v(w) < 0.8$ and the value of the function $t(w)$ can be taken as $t(w) \approx 1$ for tunneling emission with

$$w = e^{3/2}\sqrt{E_l/4\pi\varepsilon_0}/W \tag{9.6}$$

The rapidly varying, characteristic form of the $j(t)$ curve following the field cycles is illustrated in Fig. 9.4. Field emission/tunneling occurs primarily at those instants when the field strength reaches its maximum value, notably, for photoemission from metals excited with visible wavelengths. Experimental investigation of pure field

emission (i.e., $\gamma \ll 1$) is not easily realizable, since the damage threshold of bulk metal surfaces and thin films is around 10^{13} W/cm^2, which is very close to the intensity where the $\gamma \sim 1$ condition is met.

In order to investigate these processes experimentally, a practical workaround is necessary. The use of far-infrared sources has proved to be suitable for this purpose where the $\gamma \sim 1$ condition can be met at much lower intensities [31]. In addition, plasmonic field enhancement on metallic surfaces can be exploited in the visible spectral region so that the $\gamma \ll 1$ condition can be satisfied for metal films without damage. This latter method is also more advantageous due to the lack of few-cycle, ultrashort, laser sources in the far-infrared domain.

### 9.2.3.4 Strong-Field Photoemission Enhanced in Nanoplasmonic Environments

Photoemission from metals can be particularly well enhanced by plasmonic nanoparticles and the corresponding LSPs (see Fig. 9.1b). The difference, with respect to the already introduced PSPs is manyfold: (A) LSP electromagnetic fields are confined not only along one spatial dimension, but in all three. Plasmonic fields are concentrated to nanoscale volumes as small as some thousand nm^3, and they are typically localized at the sharpest features of the nanoparticles (see Fig. 9.9). (B) As a result, higher field enhancement factors can be achieved. In this case the field enhancement can be several hundreds, whereas, for propagating surface plasmons it is typically not more than twenty. This way, strong-field interactions can be induced at extremely low laser intensities. (C) The spatial distribution of these electromagnetic fields can be flexibly tailored by the nanoparticle geometry (for this, compare Fig. 9.9a, b). (D) This way, the photoemission and electron acceleration processes, as well as spatial electron distributions can also be controlled to a high degree. In order to demonstrate these potentials, we will introduce recent experimental results on this topic here [32].

The concept of our experiment is schematically illustrated in Fig. 9.10 and relies on the electron beam lithographic fabrication of plasmonic gold nanoparticles on glass substrates, illuminated by linearly polarized femtosecond laser pulses (95–110 fs duration with a central wavelength of 805 nm). These laser pulses were delivered by a long-cavity Ti:sapphire oscillator with some 200 nJ pulse energy [33–35]. After coupling the pulses into LSP oscillations of the nanoparticle sample placed in vacuum, strong-field photoemission and photoacceleration processes were investigated by time-of-flight electron spectrometry. A core element of the experimental concept was the fabrication of resonant and off-resonant nanorods with respect to the given laser wavelength, as well as of resonant bowtie nanostructures with significantly higher plasmonic field enhancement than for the nanorods. This way, both plasmonic resonance and field enhancement effects can be effectively correlated with photoemission spectra by switching between the different sample types.

Different sets of nanoparticle arrays were fabricated with 0.01 mm^2 surface area each, comprised of approximately 80,000 rod-type nanoparticles on a conductive, transparent substrate. The individual nanorods had a sufficient distance so that
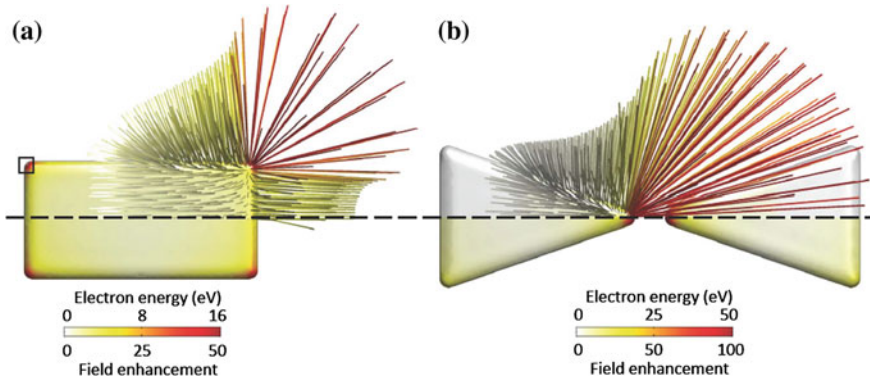
Fig. 9.9 Resonant surface plasmon generation and electron acceleration at metal nanoparticles. **a** The *colour-coded surface* in three quadrants of the nanoparticle shows the absolute value of the electric field enhancement on the nanoparticle surface. The *upper part* (above the *dashed line*) depicts the electron trajectories for one quadrant of the nanoparticles, with colour coding according to the final kinetic energies of the photoemitted and plasmonically accelerated electrons. **b** Same as panel (**a**) but for a *bowtie-shaped* nanoparticle with higher field enhancement factors. *Source* [32]
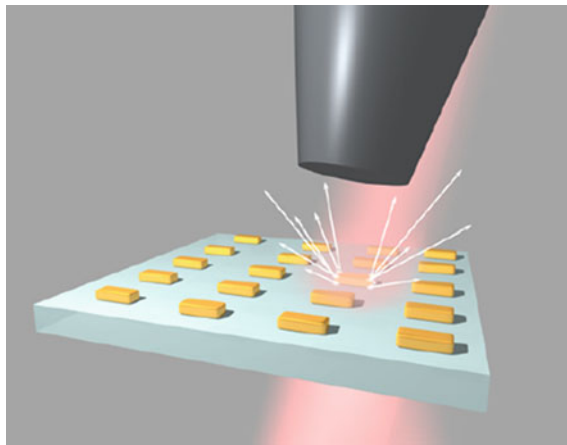
Fig. 9.10 Experimental scheme for the nanoplasmonic photoemission experiment from metal nanoparticles. Fs laser pulses are incident on a glass substrate on which arrays of metal nanoparticles were fabricated with electron beam lithography. Photoemitted electrons (*white arrows*) are analyzed by a time-of-flight spectrometer, the input opening of which is also depicted. *Source* [32]

they were not coupled electromagnetically. The nanorod height and width measured 40 and 87 nm, respectively, and the length was 120, 152 and 183 nm for three different arrays, as shown by Fig. 9.11b–d with scanning electron microscope (SEM) images. Measured optical resonances of the different nanoparticle geometries are in Fig. 9.11a. Resonances are peaked between 732 and 877 nm, representing

blue-shifted, on-resonance and red-shifted nanorods, respectively, with respect to the laser wavelength indicated with the dashed box.

Upon femtosecond illumination, electrons are generated from the nanoparticles. The spectra of these electron beams are shown in Fig. 9.11f. Remarkably, high-energy electrons with kinetic energies up to 19 eV were observed, being well above the photon energy of 1.55 eV corresponding to the laser wavelength. This indicates the presence of ponderomotive electron acceleration effects.

To confirm this hypothesis, we also carried out intensity scans of the input laser beam and recorded multiple spectra this way for all nanoparticle types involved. Results of this are shown in Fig. 9.12. It is clear from Fig. 9.12e that the cutoffs of the electron spectra scale approximately linearly with the intensity of the exciting pulses and that the highest photoemission yields and highest kinetic energies are observed from plasmonically resonant nanoparticles. They are then followed by the red-shifted and blue-shifted nanorods in this respect.

These observations are further corroborated by additional experiments performed with resonant coupled nanotriangle pairs (placed in a bowtie geometry). These closely spaced nanoparticle dimers are known to exhibit a much stronger field enhancement in the gap region between the nanotriangles. The gaps of the bowties are 20 nm wide with only a slight ±2 nm variation throughout the array. The results of the bowtie measurements, with the same experimental conditions as for the nanorods, together with the particle geometries and optical resonance properties are shown in Figs. 9.11 and 9.12 with green curves.

It is clearly visible that for the bowtie case, significantly lower incident laser intensities are sufficient to generate the same photoelectron yield and electron energies than for the nanorods. Carrying out experiments with intensities above 25 GW/cm^2 were made impossible by optical damage of the nanoparticles, also indicating higher electric field enhancement than in the case of nanorods. Similarly to nanorods, the linear scaling of the cutoff electron energies can be observed here. This scaling resembles the linear scaling of the ponderomotive energy with the intensity given in (9.1). The reason for this phenomenon will be introduced in the next sections.

### 9.2.4 Electron Acceleration Phenomena in Plasmonic Fields

As previously shown, strong laser fields can change the fundamental nature of the interaction of light with matter. It was also argued that strong fields need not necessarily be induced by intense, amplified laser pulses, PSP/LSP field enhancement can readily compensate for a substantial amount in focused laser intensity.

As already introduced, after an electron is set free by photoemission, it can undergo ponderomotive-type, cycle-by-cycle acceleration along the gradient of sharply decaying, nanolocalized electromagnetic fields. Figure 9.2c shows such a process. Here, we will analyze and show examples of this phenomenon.
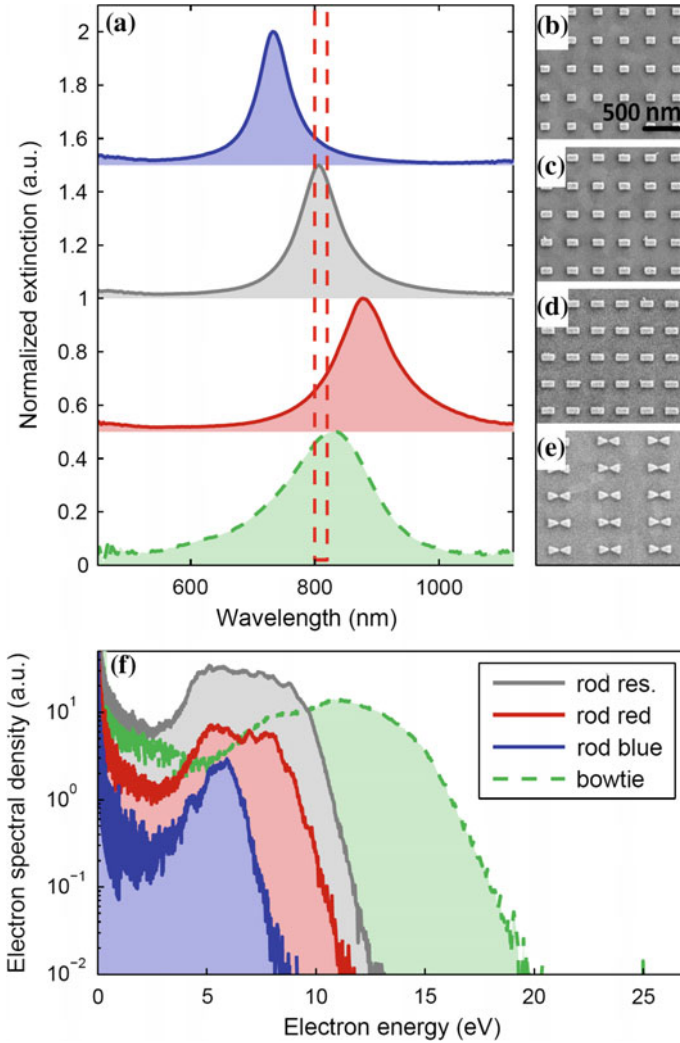
Fig. 9.11 Measured optical spectra and electron kinetic energy distributions for nanorods and bowtie nanoparticles. **a** Measured extinction spectra for nanorods with dimensions of **b** $120 \times 87 \times 40\,nm^3$, **c** $152 \times 87 \times 40\,nm^3$, and **d** $183 \times 87 \times 40\,nm^3$, which are *blue-shifted*, in resonance, and *red-shifted* with respect to the excitation bandwidth centered at $\lambda_{exc} = 805\,nm$ (see *dashed box*). Spectra are offset for clarity. The *bottom curve* in panel (**a**) depicts the spectrum for a *bowtie structure* shown in (**e**) with 90 nm width, 40 nm height, and 260 nm length (20 nm gap). **f** Electron spectra for different particle geometries and for a laser peak intensity of $25.1\,GW/cm^2$. The data below 3 eV are of limited validity due to instrumental restrictions of the time-of-flight spectrometer. *Source* [32]
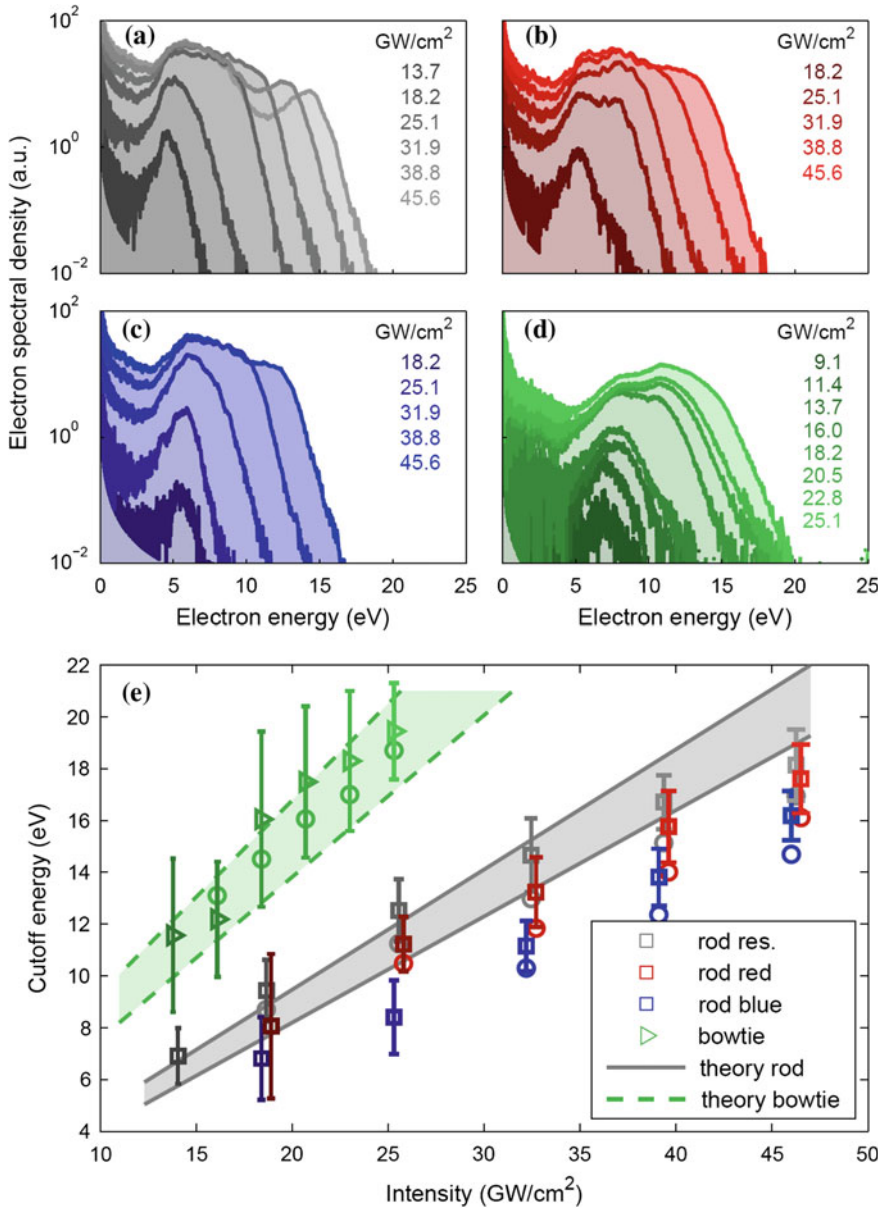
Fig. 9.12 Electron spectra as a function of peak intensity for **a** resonant rod, **b** *red-shifted* rod, **c** *blue-shifted* rod, and **d** resonant bowtie structure. **e** Cutoff energies of the electron spectra, as a function of laser intensity. The *solid* and *dashed lines* show simulation results for the resonant rod and bowtie nanoparticle, respectively. The influence of different cutoff angles $\theta_{cut} = 6$–$10°$ (accounting for the acceptance cone of the electron spectrometer) on the cutoff energies is indicated by the *shaded areas*. *Source* [32]
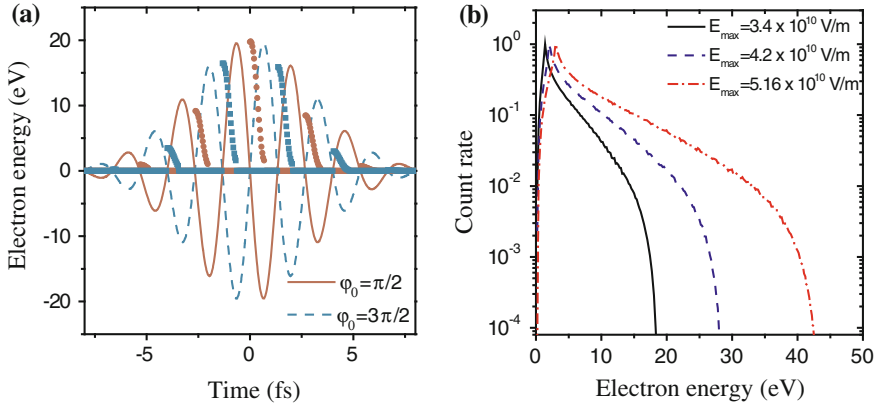
Fig. 9.13 **a** Surface-plasmon-accelerated electron energy as a function of the photoemission instant of the electrons (*scatter plots*). The electric field (with a maximum field strength of 3.4×10^{10} V/m) of the plasmon-generating 5-fs laser pulse is illustrated with *solid* and *dashed lines*. The pulse has either a "positive sine" (*solid line*) or "negative sine" waveform (*dashed line*) under the same pulse envelope. The corresponding electron energies for the "positive sine" waveform are depicted as *circles*, whereas for the "negative sine" waveform, as *squares*. **b** Electron spectra calculated for such pulses for different peak intensities of the laser pulse driving the PSP wave. *Courtesy* Péter Rácz

9.2.4.1 Fundamentals of Plasmonic Electron Acceleration

Now let us analyze the ponderomotive plasmonic electron acceleration process along a laser pulse, for different "instants of birth" of the electrons. It is obvious that the final electron kinetic energy attained in the ponderomotive acceleration process will be very highly dependent on the phase at which the electron is photoemitted and at which it starts to run a classical trajectory in the PSP/LSP field. We analyzed the final energy of electron trajectories in PSP fields by solving classical equations of motions in the field. We disregarded electrons that rescatter from the surface or those where the Lorentz force drives them toward the surface right at their "birth instant". Figure 9.13a illustrates the temporal distribution of the remaining electrons' final kinetic energies as a function of the electron photoemission instant in a maximum PSP field strength of 3.4×10^{10} V/m generated from a 5-fs-long optical pulse at 800 nm central wavelength. In this analysis, these representative, emitted electrons are collected from the central spot of the illuminated area on the metal film.

Overall, the corresponding electron kinetic energy distribution presented in Fig. 9.13 exhibits a close similarity to that of atomic electrons accelerated by an ionizing laser field [36]. However, contrary to atomic electrons, only ∼1/4 of all emission instants contribute significantly to the acceleration process in PSP field acceleration. This is due to the electron recollision and reabsorption processes. Macroscopically observable emission distributions and electron kinetic energy spectra can be numerically calculated after the assessment of a large number of trajectories with appropriate

sampling representing the whole illuminated surface and the full PSP pulse. In case of flat metal-dielectric surfaces, this method delivers a very good approximation [37]. Figure 9.13b shows full electron spectra for electron acceleration in PSP fields calculated in the above manner. Important features such as the rapid decay after the low-energy peak and the linear scaling of the spectral cutoffs with intensity (as expected from the pondermotive scaling in (9.1)) is clearly visible. These findings also highlight the mechanisms behind the spectra observed in case of LSP excitation of nanoparticles e.g. in Fig. 9.12e. In the LSP case, the contributing phenomena are completely analogous.

### 9.2.4.2 Experimental Results on Plasmonic Electron Acceleration

Apart from the enhancement of photoemission yield, PSP/LSP fields can also accelerate the electrons that are set free from the surface, thanks to the ponderomotive electron acceleration mechanism. Examples of LSP fields accelerating electrons up to 20 eV kinetic energy have been shown in Sect. 2.3.4. It was found, however, that PSP fields are more efficient when it comes to accelerating electrons to keV kinetic energies on the nanoscale.

The strength, duration, and spatial extent of the PSP evanescent plasmonic field determine the final kinetic energy gained by the electrons. Spectrally resolved measurements of PSP photoemission delivered experimental confirmation of this powerful particle acceleration mechanism several years ago [38–41]. The special feature of these electron spectra is the scaling of cutoff energies already explained above.

The first experiment to demonstrate that energetic electrons can be generated using surface plasmon waves was performed by Zawadzka et al. [38, 39]. They used a Kretschmann PSP coupling configuration and laser pulse durations of between 100 and 150 fs. They demonstrated PSP-enhanced electron spectra reaching 400 eV at a laser intensity of 40 TW/cm^2. Instead of the Kretschmann PSP coupling method, Kupersztych et al. employed a gold-coated diffraction grating to channel laser pulses into PSP waves. With this method and using 60-fs-long pulses with an 8 GW/cm^2 focused intensity, they also demonstrated PSP electron acceleration [40]. However, the highest electron energy obtained was ∼50 eV, indicating that grating coupling and PSP enhancement are much weaker compared to the Kretschmann coupling configuration.

Some 10 years ago, Irvine et al. [41] reported an even more remarkable electron energy gain by accelerating electrons in PSP fields up to 400 eV energy using merely 1.5 nJ pulse energy (focused to 1.8 GW/cm^2) delivered by a simple Ti:sapphire oscillator. However, most interesting is the fact that the PSP-enhanced electron spectrum became quasi-monoenergetic peaking at 300 eV with a FWHM of only ∼80 eV.

Further experiments were also performed by spectroscopic characterization of ultrafast plasmonic electron bunches generated and accelerated by few-cycle laser pulses [19]. This is a particularly intriguing scheme as the driver pulse duration (5 fs) was comparable to the surface plasmon lifetime. Figure 9.6 also illustrates the experimental setup used for this experiment with the only difference that the
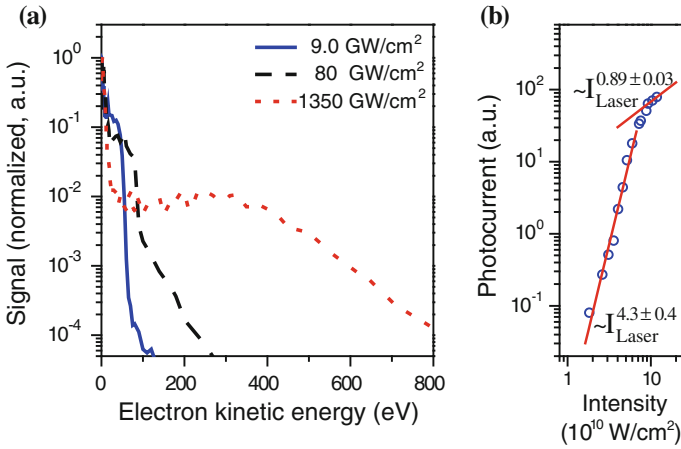
Fig. 9.14 a PSP-induced electron acceleration spectra at different incident laser intensities measured in a setup similar to that in Fig. 9.6. **b** Integrated photocurrent as a function of intensity. It shows that within the intensity range of interest in these measurements, the dominant emission mechanism changed from multi-photon-induced photoemission to tunneling emission at around 60 GW/cm^2 focused intensity

interferometer is omitted and few-cycle pulses hit the prism surface after dispersion pre-compensation with chirped mirrors. The electron detector is transformed into a retarding field spectrum analyzer by placing a grid between the prism surface and the electron multiplier tube. By changing the electron retarding voltage on the grid and measuring the signal as a function of this voltage, the integral of electron spectra can be measured easily.

This way, it was demonstrated that plasmonic-field electron acceleration can be an efficient electron energy gain technique even with few-cycle excitation. Figure 9.14 depicts the measured energy distributions at different laser intensities (measured at the surface without accounting for PSP field enhancement) where the highest focused intensity of 1.35×10^{12} W/cm^2 is slightly below the damage threshold intensity of the Ag film ($\sim 1.5 \times 10^{12}$ W/cm^2, as measured). Remarkably, energy levels approaching 1 keV can be reached within the short-lived evanescent PSP field.

9.2.5 Surface Plasmon Induced Electron Acceleration in the Mid-infrared

We have seen that in the strong-field regime, in which $\gamma \leq 1$, the ponderomotive energy becomes comparable to the electron binding energy. This regime requires typical focused laser intensities of 10^{14} W/cm^2 at 800 nm central wavelength (e.g. in case of a laser-atom interaction, without plasmonic field enhancement). Here,
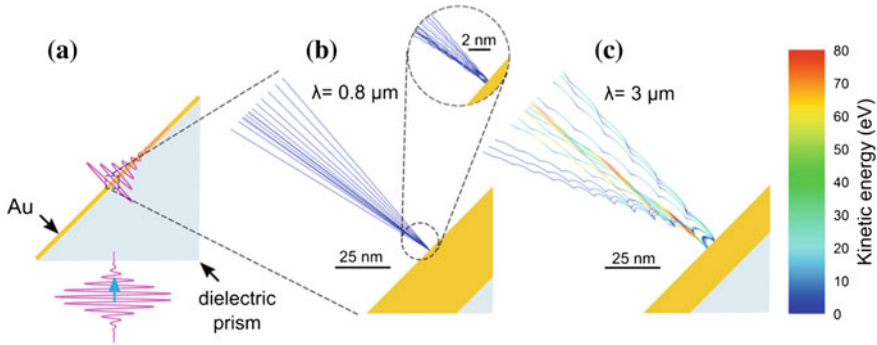
Fig. 9.15 Illustration of the concept of strong-field photoemission and electron acceleration in nanolocalized surface plasmon fields generated on thin gold films by focusing 9-cycle laser pulses in the Kretschmann-Raether coupling geometry (**a**). The advantage of using a long-wavelength mid-infrared femtosecond source is evident by depicting electron trajectories for surface plasmon excitation at (**b**) 800 nm central wavelength, 4 GW/cm^2 focused intensity and 24-fs FWHM pulses (∼9 optical cycles) and (**c**) 3 μm central wavelength, 4 GW/cm^2 focused intensity and 90-fs FWHM pulses (∼9 optical cycles). It can be seen that both the electron quiver amplitudes and the achievable kinetic energies are substantially increased in the long-wavelength case, in accordance with fundamental, ponderomotive scaling laws. *Source* [42]

we have shown how it is possible to achieve strong-field interactions at orders of magnitude lower focused intensities (40–60 GW/cm^2) by making use of PSP/LSP field enhancement. Thus, the fundamental question arises that what is the lowest intensity to attain strong-field phenomena and the corresponding electron kinetics.

We will show here that the transition between multi-photon induced (perturbative) and strong-field light-solid interactions can be shifted to unprecedentedly low focused intensities of below 1 GW/cm^2 with the help of femtosecond mid-infrared pulses and strong nanoplasmonic field confinement. Thanks to both of these effects, electron energies can be generated in a nanoscale plasmonic acceleration process that exceed the photon energy of the PSP generating pulse by almost two orders of magnitude. Accessing the strong-field regime at unprecedentedly low intensities is enabled by the usage of a mid-infrared femtosecond source. This way one can exploit the $1/\lambda$ scaling of the Keldysh-parameter and the λ^2 scaling of the ponderomotive energy of the electrons. The concept and the corresponding scalings are illustrated in Fig. 9.15 showing numerical, semi-classical simulations of the plasmonic photoemission and electron acceleration phenomenon involving PSPs on a metal thin film.

For these experiments, we used a mid-infrared optical parametric chirped pulse amplifier (OPCPA) source [43] delivering 90 fs pulses at a central wavelength of 3.1 μm. These pulses were loosely focused onto the hypotenuse face of a right-angle CaF$_2$ prism where they were efficiently coupled to PSPs on a 15 nm thick film of gold. Plasmonic photocurrent and surface plasmon enhanced photoemission spectra were then measured with a retarding grid analyzer followed by an electron multiplier.
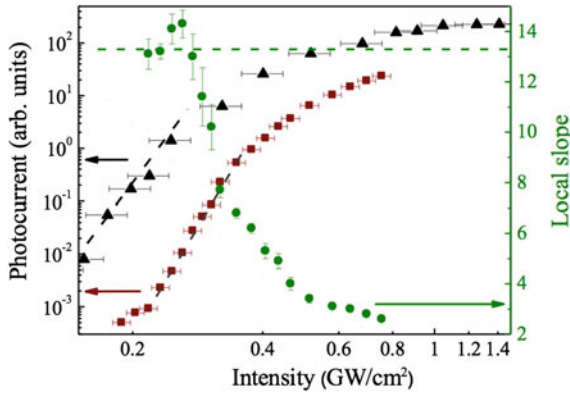
Fig. 9.16 Focused laser intensity dependence of the total plasmonic photocurrent for two independent exemplary scans (offset for clarity, *black triangles* and *red squares*). Spot sizes (FWHM) of 870 μm (*black triangles*) and 1400 μm (*red squares*) were used and the pulse energy was varied as described in the main text. The slopes of the fits to the initial sections are 12.3 ± 1.8 and 13.1 ± 0.6, respectively. The local slope of the second curve is also plotted (*green circles*) to illustrate the gradual transition between multi-photon-induced and tunneling (strong-field) photoemission at very low laser intensities. The electron multiplier gain of each measurement was set such that for the maximum intensity the signal did not show a saturated trace on an oscilloscope. After that, quantitative voltage signal was acquired with a lock-in amplifier. *Source* [42]

Two independent measurements of the intensity dependence of the plasmonic photocurrent are depicted in Fig. 9.16 on a double logarithmic scale. We controlled the intensity by varying the pump power of the last amplifier stage in the OPCPA. This procedure did not lead to modifications of the temporal profile of the pulse. The curves in Fig. 9.16 show that the total photocurrent first scales highly nonlinearly with the intensity (according to a ∼13th power law), as expected. Here, multi-photon induced photoemission with a photon energy of 0.4 eV takes place and the work function is ∼5.1 eV for polycrystalline gold. The power-law scaling behaviour substantially changes at around 0.6 GW/cm² focused intensity where the local slopes of the curve start to become reduced. This is a well-known signature of the transition to tunnelling, however, it takes place here at unprecedentedly low intensities, suggesting strong field enhancement of PSPs.

To determine the magnitude of the field enhancement responsible for this tunneling transition, one can also measure the electron spectra for a number of incident laser intensities and evaluate the spectral cutoffs, as shown in Fig. 9.17a. One can see that whereas the ponderomotive energy of electrons according to (9.1) is only between 1.3 and 3.1 meV for the incident laser intensities, orders of magnitude higher electron energies can be achieved in the PSP field. Analyzing maximum kinetic energies of the spectra, i.e. the cutoffs, we find cutoff values of up to 47 eV.

With the same setup, independent measurements of the maximum (cutoff) kinetic energy of the electrons as a function of intensity were carried out, without resolving electron spectra. This could be achieved by increasing the retardation field and
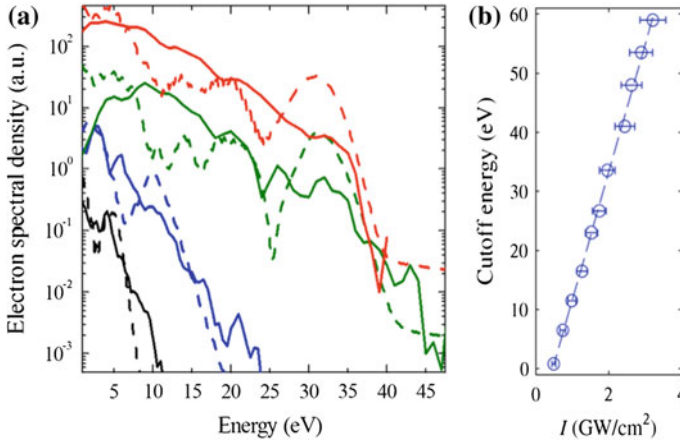
Fig. 9.17 a Plasmonic photoemission electron spectra for intensities 1.4 GW/cm^2 (*black*), 1.7 GW/cm^2 (*blue*), 2.8 GW/cm^2 (*green*) and 3.5 GW/cm^2 (*red*) in the strong-field photoemission regime. The evaluated plasmonic field enhancement factors are between 28 and 34. *Dashed lines* show the spectra calculated from the quantum mechanical model involving a plasmonic field enhancement factor. Note that the respective spectra are offset along the *y* axis for clarity. **b** Maximum kinetic energy of plasmonically accelerated photoelectrons as a function of focused laser intensity as an independent measurement. For a given intensity we increased the retardation field until the noise level was reached, being equivalent to the signal without any beam incident on the prism. The linear dependence of cutoff on intensity confirms the classical ponderomotive scaling law. All measurements were carried out with a spot size (FWHM) of 870 μm and the pulse energy was varied as described in the main text. *Source* [42]

monitoring the voltage where the electron multiplier signal reached the noise level. These results (shown in Fig. 9.17b) confirm that the electron acceleration process in the enhanced PSP field is governed by the classical ponderomotive scaling law. According to (9.1), the maximum kinetic energy of electrons should be proportional to $I\lambda^2$ and this linear scaling with the intensity is observed clearly in the same intensity range as that of Fig. 9.16. Since the acceleration process is independent of the photoemission mechanism, a linear intensity dependence is observed irrespective of the multiphoton or strong-field nature of the emission process.

The experimentally determined cutoff values in Fig. 9.17a allow one to determine the maximum field enhancement factor at the plasmonic thin film in the following way. It is known that the highest energy electrons undergo rescattering on the surface after a fraction of the light oscillation cycle [44–46]. Provided that the emission and rescattering events take place at the most favorable phases of the oscillating electromagnetic field, the electron can gain a kinetic energy amounting to as much as ten times the ponderomotive potential [45, 46]. Thus, by evaluating the cutoffs of the measured spectra, we can determine the maximum value of the ponderomotive potential within the focal spot. The cutoff scaling law is universally valid irrespective of the medium, i.e. atom, surface, etc., and thus it is applicable here, too. Since rescattering takes place within a half cycle of the field and this initial phase of electron

motion takes place within the closest nanoscale proximity of the surface (see e.g. Fig. 9.15), one can measure the highest local field enhancement factor experimentally.

Carrying out this analysis with the measured cutoff values (see Fig. 9.17a), one finds an increase of the cutoff by three orders of magnitude compared to the values expected from the focused intensities (see (9.1)) and the mentioned $10 \times U_p$ cutoff law. This shows that a high effective field enhancement factor is present, provided by the plasmonic thin film. The observed cutoff increase corresponds to field enhancement factors between 28 and 37 for the analysed spectra. It has to be noted that the maximum field enhancement factor of a perfectly flat gold film with 15 nm thickness is 19 at this wavelength. We attribute the somewhat higher measured values to additional surface roughness of the metal film [47].

In order to confirm these conclusions from a quantum mechanical point-of-view, one can also carry out a theoretical analysis of the strong-field light-matter interaction the results of which are shown in Fig. 9.17a with dashed lines. The theoretical model used has already been described and employed for the calculation of the electron photoemission from metal nanotips [48]. To match the cutoff energies of a given experimental electron spectrum, one can use the experimental intensity and vary the field enhancement factor in the simulation, representing the only fit parameter in this case. The parameters used for the plots in Fig. 9.17a agree to within a factor of two with the experimentally determined enhancement factors. Best-match modeled electron spectra in Fig. 9.17a yielded field enhancement factors of between 60 and 70, representing higher enhancement values than those gained by the cutoff evaluation of measured spectra. This is, however, a satisfactory agreement on the magnitude of the field enhancement in this particular configuration taking into account the limitations of the quantum mechanical model used.

In conclusion, it was demonstrated that with the help of PSP field enhancement and long excitation wavelengths, one can achieve strong-field light-matter interaction at extremely low incident laser intensities, opening a new paradigm in strong-field physics. High electron energies exceeding the ponderomotive energy in the incident light field by several orders of magnitude were achieved in an all-plasmonic electron acceleration scheme within the closest nanoscale proximity of the metal film.

9.3 Conclusions and Outlook

The generation of surface plasmons at metal-vacuum interfaces (PSPs) and in nanoparticles (LSPs) is known to confine the electromagnetic energy to subwavelength spatial dimensions either along one (PSPs) or along all three (LSPs) spatial coordinates. This electric field confinement, along with the high field enhancement, result in a number of intriguing phenomena including strong-field interactions at unprecedentedly low intensities (some GW/cm^2) and electron acceleration gradients exceeding a few GeV/m. The generation of high-energy, ultrashort electron bunches by using low-intensity, compact lasers can open the doorway for novel time-resolved

investigations, as well. The high plasmonic field confinement allows access to strong-field interactions, which, until recently, has been the terrain of multi-TW lasers.

The detailed investigation of ultrafast plasmonic electron acceleration in PSP fields brought important discoveries in recent years which involved a large number of novel features such as all-optical, keV electron acceleration on the nanoscale or strong-field plasmonic photoemission. In addition, photoemitted and photoaccelerated electrons can be used to characterize few-cycle surface plasmon wavepackets. The findings discussed here, supported with experimental observations, focused on the ultrafast physics phenomena involved in the photoemission mechanisms of electrons in strong nanoplasmonic fields and acceleration of freely propagation electrons on the nanoscale. By exploiting PSP/LSP field enhancement, plasmon-induced tunneling emission from the metal surface at low laser intensity was demonstrated.

Controlling localized surface plasmon fields via both the shape of the optical pulse and the nanostructure geometry provide an additional method of optical control of the interaction processes involved. By tailoring the nanostructures' interaction with the laser, ultrafast electron processes can be exploited for a number of applications including extreme ultraviolet light generation [49] and the construction of nanostructured plasmonic photocathodes [50, 51]. The investigation of ultrafast strong-field plasmonic phenomena can be viewed as a natural route that will ultimately take us to the observation of many fundamental processes in nature involving biochemical reactions, molecular, lattice and collective electron dynamics, as well as their coherent control via shaping electric field evolution and distribution on the nanoscale.

References

1. K. Kneipp et al., Single molecule detection using surface-enhanced Raman scattering (SERS) Phys. Rev. Lett. **78**, 1667–1670 (1997)
2. S. Lal, S. Link, N.J. Halas, Nano-optics from sensing to waveguiding. Nat. Photon. **1**, 641–648 (2007)
3. H.J. Simon, D.E. Mitchell, J.G. Watson, Optical second-harmonic generation with surface plasmons in silver films. Phys. Rev. Lett. **33**, 1531–1534 (1974)
4. J.C. Quail, J.G. Rako, H.J. Simon, R.T. Deck, Optical second-harmonic generation with long-range surface plasmons. Phys. Rev. Lett. **50**, 1987–1990 (1983)
5. D. Polyushkin, I. Márton, P. Rácz, P. Dombi, E. Hendry, W.L. Barnes, Mechanisms of THz generation from silver nanoparticle and nanohole arrays illuminated by 100 fs pulses of infrared light. Phys. Rev. B **89**, 125–426 (2014)
6. H. Raether, *Surface Plasmons on Smooth and Rough Surfaces and on Gratings* (Springer-Verlag, Berlin, 1988)
7. J.A. Schuller et al., Plasmonics for extreme light concentration and manipulation. Nat. Mater. **9**, 193–204 (2010)
8. H. Atwater, The promise of plasmonics. Sci. Am. **296**, 56–63 (2007)
9. S.A. Maier, *Plasmonics: Fundamentals and Applications* (Springer, Berlin, 2007)

10. J.N. Anker, W.P. Hall, O. Lyandres, N.C. Shah, J. Zhao, R.P. Van Duyne, Biosensing with plasmonic nanosensors. Nat. Mater. **7**, 442–453 (2008)

11. D. Koller, A. Hohenau, H. Ditlbacher, N. Galler, F. Reil, F.R. Aussenegg, A. Leitner, E. List, J.R. Krenn, Organic plasmon-emitting diode. Nat. Photon. **2**, 684–687 (2008)

12. A.L. Falk, F.H.L. Koppens, C.L. Yu, K. Kang, N. de Leon Snapp, A.V. Akimov, M.-H. Jo, M.D. Lukin, H. Park, Near-field electrical detection of optical plasmons and single-plasmon sources. Nat. Phys. **5**, 475–479 (2009)

13. V.E. Ferry, L.A. Sweatlock, D. Pacifici, H.A. Atwater, Plasmonic nanostructure design for efficient light coupling into solar cells. Nano Lett. **8**, 4391–4397 (2008)

14. T. Tsang, T. Srinivasan-Rao, J. Fischer, Surface-plasmon-enhanced multiphoton photoelectric emission from thin silver films. Opt. Lett. **15**, 866–868 (1990)

15. T. Tsang, T. Srinivasan-Rao, J. Fischer, Surface-plasmon field-enhanced multiphoton photo-electric emission from metal films. Phys. Rev. B **43**, 8870–8878 (1991)

16. S.E. Irvine, Laser-field femtosecond electron pulse generation using surface plasmons. Ph. D. Thesis, University of Alberta, Canada (2006)

17. C. Lemell, X.-M. Tong, F. Krausz, J. Burgdörfer, Electron emission from metal surfaces by ultrashort pulses: determination of the carrier-envelope phase. Phys. Rev. Lett. **90**, 076403 (2003)

18. H. Petek, S. Ogawa, Femtosecond time-resolved two-photon photoemission studies of electron dynamics in metals. Prog. Surf. Sci. **56**, 239–310 (1997)

19. P. Dombi et al., Observation of few-cycle, strong-field phenomena in surface plasmon fields. Opt. Express **18**, 24206 (2010)

20. W.S. Fann, R. Storz, J. Bokor, Observation of above-threshold multiphoton photoelectric emission from image potential surface states. Phys. Rev. B **44**, 10980 (1991)

21. G. Farkas et al., Above-threshold multiphoton photoelectric effect of a gold surface. Opt. Eng. **32**, 2476 (1993)

22. M. Aeschlimann et al., Observation of surface enhanced multiphoton photoemission from metal surfaces in the short pulse limit. J. Chem. Phys. **102**, 8606 (1995)

23. F. Bisio et al., Mechanisms of high-order perturbative photoemission from Cu(001). Phys. Rev. Lett. **96**, 087601 (2006)

24. F. Banfi et al., Experimental evidence of above-threshold photoemission in solids. Phys. Rev. Lett. **94**, 037601 (2005)

25. P. Agostini et al., Free-free transitions following six-photon ionization of xenon atoms. Phys. Rev. Lett. **42**, 1127 (1979)

26. P. Hommelhoff, Y. Sortais, A. Aghajani-Talesh, M.A. Kasevich, Field emission tip as a nanometer source of free electron femtosecond pulses. Phys. Rev. Lett. **96**, 077401 (2006)

27. R. Bormann et al., Tip-enhanced strong-field photoemission. Phys. Rev. Lett. **105**, 147601 (2010)

28. B. Piglosiewicz et al., Carrier-envelope phase effects on the strong-field photoemission of electrons from metallic nanostructures. Nat. Phot. **8**, 37–42 (2014)

29. M. Schenk, M. Krüger, P. Hommelhoff, Strong-field above-threshold photoemission from sharp metal tips. Phys. Rev. Lett. **105**, 257601 (2010)

30. V.T. Binh, N. Garcia, S.T. Purcell, Electron field emission from atom-sources: fabrication, properties, and applications of nanotips. Adv. Imaging Electron Phys. **95**, 63 (1996)

31. G. Farkas, S.L. Chin, P. Galarneau, F. Yergeau, A new type of intense CO_2 laser induced electron emission from a gold surface. Opt. Comm. **48**, 275 (1983)

32. P. Dombi et al., Ultrafast strong-field photoemission from plasmonic nanoparticles. Nano Lett. **13**, 674–678 (2013)

33. P. Dombi, P. Antal, Invetisgation of a 200-nJ chirped-pulse Ti: sapphire oscillator for white light generation. Laser Phys. Lett. **4**, 538 (2007)

34. P. Dombi, P. Antal, J. Fekete, R. Szipöcs, Z. Várallyay, Chirped-pulse supercontinuum generation with a long-cavity Ti: sapphire oscillator. Appl. Phys. B **88**, 379 (2007)

35. J. Fekete, P. Rácz, P. Dombi, Compression of long-cavity Ti:sapphire oscillator pulses with large-mode-area photonic crystal fibers. Appl. Phys. B **111**, 415–418 (2013)

36. G. Reider, XUV attosecond pulses: generation and measurement. J. Phys. D **37**, R37–R48 (2004)
37. P. Dombi, P. Rácz, B. Bódi, Surface-plasmon enhanced electron acceleration with few-cycle laser pulses. Laser Part. Beams **27**, 291 (2009)
38. J. Zawadzka, D. Jaroszynski, J.J. Carey, K. Wynne, Evanescent-wave acceleration of femtosecond electron bunches. Nucl. Instr. Meth. Phys. Res. A **445**, 324–328 (2000)
39. J. Zawadzka, D. Jaroszynski, J.J. Carey, K. Wynne, Evanescent-wave acceleration of ultrashort electron pulses. Appl. Phys. Lett. **79**, 2130–2132 (2001)
40. J. Kupersztych, P. Monchicourt, M. Raynaud, Ponderomotive acceleration of photoelectrons in surface-plasmon-assisted multiphoton photoelectric emission. Phys. Rev. Lett. **86**, 5180–5183 (2001)
41. S.E. Irvine, A. Dechant, A.Y. Elezzabi, Generation of 0.4-keV femtosecond electron pulses using impulsively excited surface plasmons. Phys. Rev. Lett. **93**, 184801 (2004)
42. S.M. Teichmann, P. Rácz, M. Ciappina, J.A. Pérez-Hernandez, A. Thai, J. Fekete, L. Veisz, J. Biegert, P. Dombi, Strong-field plasmonic photoemission in the mid-IR $< 1GW/cm^2$ at intensity, Sci. Rep. **5**, 7584 (2015)
43. O. Chalus, A. Thai, P.K. Bates, J. Biegert, Six-cycle mid-infrared source with 3.8 μJ at 100 kHz. Opt. Lett. **35**, 3204–3206 (2010)
44. C. Farkas, C. Tóth, A. Köházi-Kis, Above-threshold multiphoton photoelectric effect of a gold surface. Opt. Eng. **32**, 2476–2480 (1993)
45. G.G. Paulus, W. Becker, W. Nicklich, H. Walther, Rescattering effects in above-threshold ionization: a classical model. J. Phys. B: At. Mol. Opt. Phys. **27**, L703–L708 (1994)
46. P. Rácz, S.E. Irvine, M. Lenner, A. Mitrofanov, A. Baltuska, A.Y. Elezzabi, P. Dombi, Strong-field plasmonic electron acceleration with few-cycle, phase-stabilized laser pulses. Appl. Phys. Lett. **98**, 111116 (2011)
47. P. Rácz, S.E. Irvine, M. Lenner, A. Mitrofanov, A. Baltuska, A.Y. Elezzabi, P. Dombi, Strong-field plasmonic electron acceleration with few-cycle, phase-stabilized laser pulses. Appl. Phys. Lett. **98**, 111116 (2011)
48. M. Krüger, M. Schenk, M. Föster, P. Hommelhoff, Attosecond physics in photoemission from a metal nanotip. J. Phys. B **45**, 074006 (2012)
49. I. Park, K. Seungchul, C. Joonhee, D.H. Lee, Y.J. Kim, M.F. Kling, M.I. Stockman, S.W. Kim, Plasmonic generation of ultrashort extreme-ultraviolet light pulses. Nat. Photon. **5**, 677 (2011)
50. W.S. Graves, F.X. Kartner, D.E. Moncton, P. Piot, Intense superradiant X rays from a compact source using a nanocathode array and emittance exchange. Phys. Rev. Lett. **108**, 263904 (2012)
51. R.K. Li, H. To, G. Andonian, J. Feng, A. Polyakov, C.M. Scoby, K. Thompson, W. Wan, H.A. Padmore, P. Musumeci, Surface-plasmon resonance-enhanced multiphoton emission of high-brightness electron beams from a nanostructured copper cathode. Phys. Rev. Lett. **110**, 074801 (2013)